Journal of Power Sources 196 (2011) 6802–6808

Contents lists available at ScienceDirect

Journal of Power Sources

journal homepage: www.elsevier.com/locate/jpowsour

# Investigation on porous MnO microsphere anode for lithium ion batteries

Kaifu Zhong[a], Bin Zhang[a], Shihai Luo[b], Wen Wen[b], Hong Li[a,*], Xuejie Huang[a], Liquan Chen[a]

[a] Institute of Physics, Chinese Academy of Sciences, Beijing 100190, China
[b] Shanghai Synchrotron Radiation Facility, Chinese Academy of Sciences, Pudong New Area, Shanghai 201204, China

ARTICLE INFO

*Article history:*
Received 16 September 2010
Accepted 10 October 2010
Available online 16 October 2010

*Keywords:*
Manganese monoxide
Li-ion batteries
X-ray absorption near edge structure
Extended X-ray absorption fine structure
Thermodynamics
Kinetics

ABSTRACT

MnO microspheres with and without carbon coating are prepared as anode materials for lithium ion batteries. The MnO microsphere material shows a reversible capacity of 800 mAh $g^{-1}$ and an initial efficiency of 71%. It can deliver 600 mAh $g^{-1}$ at a rate of 400 mA $g^{-1}$. Results of Mn K-edge X-ray absorption near-edge structure (XANES) spectra and extended X-ray absorption fine structure (EXAFS) confirm further the conversion reaction mechanism, indicate that pristine MnO is reduced to $Mn^0$ after discharging to 0 V and part of reduced $Mn^0$ is not oxidized to $Mn^{2+}$ after charging to 3 V. This explains the origin of the initial irreversible capacity loss partially. The quasi open circuit voltage and the relationship between the current density and the overpotential are investigated. Both indicate that there is a significant voltage difference between the charging and discharging profiles even when the current density decreases to zero.



## 1. Introduction

Lithium ion batteries are the most preferred power sources for portable electronic devices and electric vehicles due to high gravimetric and volumetric energy densities. Graphite has been used widely as negative electrode material because of its high specific capacity (~300–350 mAh $g^{-1}$), good cyclic performance (500–1000 cycles), high columbic efficiency (initial efficiency > 92%, efficiency in successive cycles > 99.5%), reasonable rate performance (capacity retention of 80% at 3*C*), low cost and environmental friendly feature. Great efforts have been made on exploring high capacity anode materials to replace graphite. Besides Si or Sn, which contain active component to form alloy with lithium, transition metal (TMX) compounds can store lithium through conversion reaction reversibly and have attracted wide attention as high capacity anode materials for Li-ion batteries [1–10].

Among TMX, MnO is quite attractive as anode material due to its relatively low electromotive force (emf) (1.032 V vs. $Li^+/Li$). Lithium storage in MnO powder electrode has been studied firstly by Poizot et al. [4]. Their results indicate that the MnO powder electrode could be discharged and charged under a very small current density (1/300*C*) by a potential static intermittent titration technique (PITT) mode. Recently, Yu et al. found that the MnO thin film electrode showed high volumetric capacity (>3485 mAh $cm^{-3}$ at 0.125*C*), relative low polarization (voltage difference between charge and discharge, ~0.7 V at 0.125*C*) and reasonable rate performances (50% capacity retention at 6*C*) [11]. Zhong et al. demonstrated that the MnO powder electrode showed high specific capacity (650 mAh $g^{-1}$ at 0.06*C*), preferable rate performance (60% capacity retention at 0.5*C*) and relatively low polarization (~0.7 V at 0.06*C*) [12]. Liu et al. reported a MnO/C nanocomposite material which showed 680 mAh $g^{-1}$ reversible capacity and 196 mAh $g^{-1}$ capacity at a current density of 1600 mA $g^{-1}$ [13]. Besides high reversible capacity and reasonable rate performance, MnO possesses abundant source, low cost and environmental friendly features. The main barriers for practical application are the low initial columbic efficiency (<70%) and high voltage polarization, needing great improvement [11,12].

According to *ex situ* TEM and XRD observations on MnO electrode at different lithiated states, it has been confirmed that lithium is stored in MnO reversibly mainly through the conversion reaction mechanism at higher voltage (>1.0 V) and the interfacial charging mechanism at lower voltage (<1.0 V) [12]. Initial polycrystalline MnO converted into an amorphous structure after a full insertion of lithium. Then the nanocomposite partially converted back into nanocrystalline MnO upon lithium extraction [12]. Such a variation in microstructure has also been observed in many transitional metal compounds occurring the conversion reactions [1,2,9].

Although the electrochemical reaction formula of MnO with lithium can be written unambiguously [12], detailed microstructure and chemical state of Mn during lithiation and delithiation are still not very clear. Such information, together with other findings, could be essential to determine and understand origin of the large initial irreversible capacity loss, thermodynamic and kinetic behaviors.

In this paper, MnO microspheres have been prepared and coated with carbon further. By this approach, initial efficiency and rate per-

* Corresponding author. Tel.: +86 10 82648067; fax: +86 10 82649046.
*E-mail address:* hli@aphy.iphy.ac.cn (H. Li).

0378-7753/$ – see front matter © 2010 Elsevier B.V. All rights reserved.
doi:10.1016/j.jpowsour.2010.10.031

formance are improved further. In addition, the local structure and valence variation of Mn in the conversion reaction are studied further by synchrotron X-ray absorption fine structure spectroscopy (XAS). Finally, thermodynamic and kinetic feature of MnO anode are also discussed.

## 2. Experimental

$MnCO_3$ microspheres were prepared firstly. Typically, $MnSO_4$ (0.02 mol $L^{-1}$) and $NH_4HCO_3$ (0.2 mol $L^{-1}$) were separately dissolved in water (100 mL). Ethanol (20 mL) was then added into the $MnSO_4$ solution with stirring. After complete dispersion, the $NH_4HCO_3$ solution was quickly added into the mixture at 4 °C. After 2 min, the solution turned white and the mixture was maintained at 4 °C for 2 h. Obtained material was separated by centrifugation and washed several times with ultrapure water and ethanol and dried at room temperature in a vacuum oven.

Porous MnO microspheres were obtained by decomposing $MnCO_3$ under argon atmosphere at 600 °C for 1 h. Through chemical vapor deposition using toluene as carbon source and argon atmosphere as gas carrier with a flow rate of 100 sccm (standard cubic centimeter per minute), porous carbon coated MnO microsphere powder was obtained at 700 °C for 4 h.

The test electrode was composed of active material (82.5 wt%), carbon black (7.5 wt%) and polyvinylidene fluoride (PVDF) (10 wt%). Cu foil was used as the current collector, Li foil was used as the counter electrode and 1 M $LiPF_6$ dissolved in a mixture of ethylene carbonate (EC) and dimethyl carbonate (DMC) (1:1, V/V) (Shanghai Topsol Ltd., $H_2O$ <10 ppm) was used as the electrolyte. A Swagelok-type two-electrode cell was constructed for electrochemical test. The cell was assembled in an argon-filled glove box and cycled between 10 mV and 3 V using a land automatic battery tester by charging/discharging the cell at a rate of 50 mA $g^{-1}$ in most of cases.

The material was characterized by a X'Pert Pro MPD X-ray diffractometer (Philips, Holland) using Cu Kα1 radiation (λ = 1.5405 Å), and a scanning electron (SEM) microscope (XL 30 S-FEG, FEI Co., 10 kV). The Raman spectra were recorded by a Horiba Jobin Yvon LabRAM HR800 Raman Microscope under ambient conditions at room temperature with a spectra-Physics $Ar^+$ laser. Typically, about 0.1 mW of 532 nm line of the argon ion laser was used. *Ex situ* Mn *K*-edge XAS spectra were collected at beamline BL14W of Shanghai Synchrotron Radiation Facility in the transmission mode. Si (1 1 1) double crystal monochromator was employed to monochromatized the beam. The XAS data was further analyzed using the IFEFFIT program [14].

## 3. Results and discussion

### 3.1. Sample characterization

The XRD patterns of obtained samples are shown in Fig. 1. Pure rhombohedral $MnCO_3$ (JCPDS 44-1472) and face centered cubic MnO (JCPDS card No. 78-0424) are obtained. Grain size of obtained $MnCO_3$ is 36 nm estimated roughly by Scherrer equation using Jade software. Grain sizes of two MnO samples are 50 nm and 48 nm respectively.

Fig. 2a and b presents typical SEM images of obtained $MnCO_3$ material. It shows a dense spherical morphology with a uniform size distribution ranging from 2 to 3 μm. The surface of as-prepared $MnCO_3$ microspheres is composed of tiny grains. After heating under argon atmosphere at 600 °C for 1 h, $MnCO_3$ decomposes into MnO microspheres. The particle size is around 2–3 μm. Each particle is composed of 50–100 nm primary particles, as shown in Fig. 2c and d. In order to improve the electron conductivity, carbon coating was performed through a chemical vapor deposition (CVD) treatment using toluene as carbon source. As shown in Fig. 2e and f, the morphology is similar as uncoated porous MnO microspheres (for convenience, uncoated MnO sample is named as the MnO sample, carbon coated sample is named as the C/MnO sample).

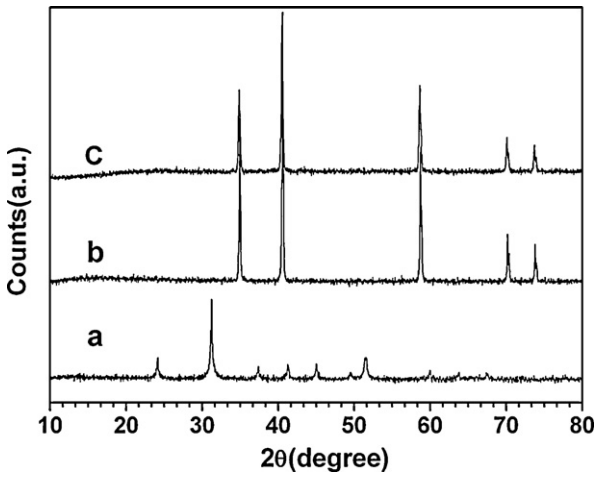


**Fig. 1.** XRD patterns of MnO samples: (a) $MnCO_3$, (b) MnO, and (c) C/MnO.

Raman spectra of the MnO sample and the C/MnO sample are shown in Fig. 3. According to the literatures, the band at 648 $cm^{-1}$ is related to the electronic excitation of impurity in MnO and the band at 544 $cm^{-1}$ is assigned to two-TO phonon scattering [15]. The bands below 400 $cm^{-1}$ have not been explained clearly in the literatures, might be from minor $Mn_3O_4$ on surface [16,17]. The broad hump around 1000 $cm^{-1}$ could be originated from TO + LO mode or 2LO modes [18]. After carbon coating, the bands at 544 $cm^{-1}$ and 306 $cm^{-1}$ disappear. The reason is not clear. And two bands at 1353 $cm^{-1}$ and 1586 $cm^{-1}$ appear, which are D-band and G-band of carbon, indicating the existence of carbon coating layer.

### 3.2. Electrochemical performance of MnO electrode

Charging and discharging curves of the MnO and the C/MnO electrode are compared in Fig. 4a and b. The reversible capacities for the two samples at the second cycle are about 821 mAh $g^{-1}$ and 760 mAh $g^{-1}$ and the initial columbic efficiencies are 71% and 72%, respectively. Both reversible capacity and initial efficiency are improved compared to our previous report of carbon coated irregular MnO powder material, which showed a reversible capacity of 650 mAh $g^{-1}$ and an initial columbic efficiency of 65% [12]. It has to be mentioned that the theoretical capacity of lithium storage in MnO through full conversion reaction is 698 mAh $g^{-1}$. As we have discussed before, lithium storage below the emf value (1.032 V) through the interfacial charging mechanism contributes a reversible capacity of 200 mAh $g^{-1}$, as seen in the charging profiles in Fig. 4. Therefore, the reversible capacities from the conversion reaction are about 620 mAh $g^{-1}$ and 560 mAh $g^{-1}$ for the two samples. This indicates apparently that part of formed $Li_2O$/Mn nanocomposite does not fully convert back to MnO during charging to 3 V.

The voltage profiles of the two samples are quite similar. In order to compare the polarization of the two samples, the differential capacity curves are also shown in Fig. 4c and d. The peak positions in the curves and the difference values between the peak voltages at the first cycle and at the second cycle are listed in Table 1. Accordingly, the voltage polarization of the C/MnO sample is slightly smaller than the MnO sample. For both samples, the voltage difference between the second discharge and the first discharge is about 0.45 V while the voltage difference between the second charge and the first charge is less than 0.05 V. This indi-

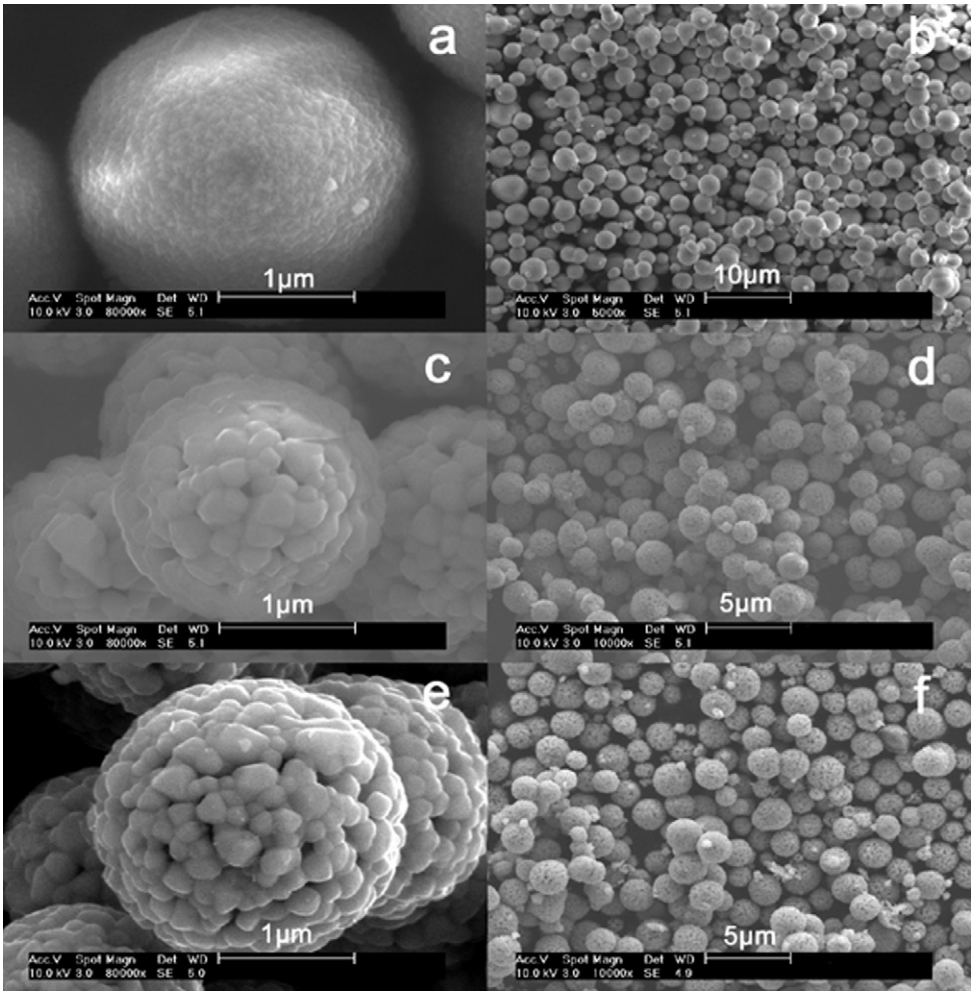


**Fig. 2.** High-magnification and low-magnification SEM. (a and b) $MnCO_3$, (c and d) MnO obtained by decomposing $MnCO_3$ under argon atmosphere at 600 °C for 1 h, (e and f) C/MnO through chemical vapor deposition using toluene as carbon source at 700 °C for 4 h.

cates that there is a large polarization variation for the MnO and the C/MnO electrode after the first discharge. Another issue can be seen that there is a large voltage difference between the second charge and the second discharge. This voltage hysteresis is about 0.64 V for the MnO electrode and the 0.61 V for the C/MnO electrode. High voltage hysteresis is a common feature for conversion reactions. Relatively speaking, MnO-based materials show relatively lower voltage hysteresis among other transitional metal compounds [12].

For an ideal conversion reaction, presuming the charging overpotential is the same as the discharging overpotential, then the emf value can be estimated roughly from the middle point between the charging curve and the discharging curve ($E_{d2}$+($E_{c2} - E_{d2}$)/2). This value is 0.91 and 0.95 V, respectively, for the two samples. The theoretical emf value of the conversion reaction of bulk MnO with lithium is 1.032 V vs. $Li^+$/Li. The existence of such a difference is partially related to the contribution of the interfacial charging mechanism and deviation from the ideal bulk thermodynamic property, which will be discussed in later section.

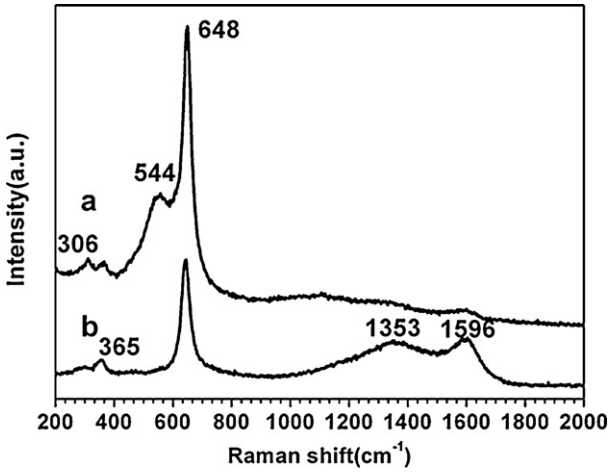


**Fig. 3.** Raman spectra of MnO sample. (a) MnO and (b) C/MnO.

**Table 1**
Polarization analysis on galvanostatic voltage profiles.

| Voltage (V) | $E_{d1}$ | $E_{c1}$ | $E_{d2}$ | $E_{c2}$ | $\Delta E_{d2-d1}$ | $\Delta E_{c2-c1}$ | $\Delta E_{c2-d2}$ | $E_{d2} + \Delta E_{c2-d2}/2$ |
|---|---|---|---|---|---|---|---|---|
| MnO | 0.136 | 1.23 | 0.617 | 1.26 | 0.481 | 0.03 | 0.64 | 0.912 |
| C/MnO | 0.192 | 1.21 | 0.649 | 1.26 | 0.457 | 0.05 | 0.61 | 0.954 |

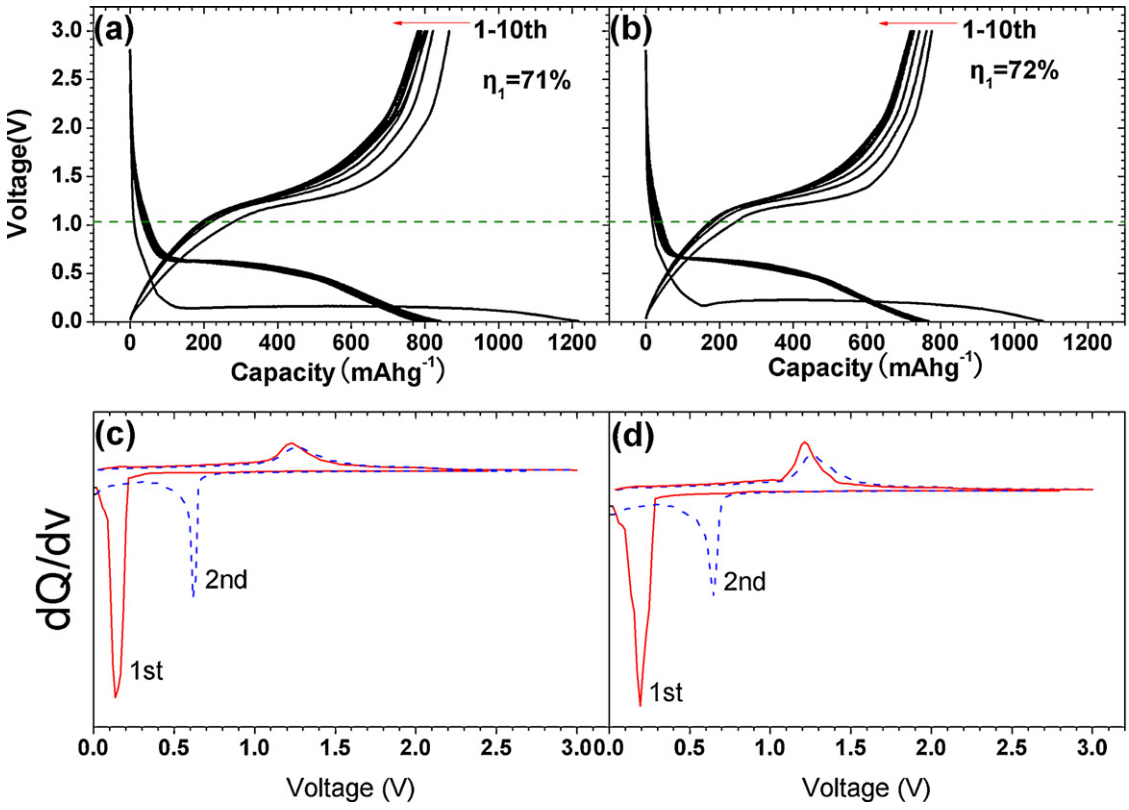


**Fig. 4.** Charging and discharging curves of the MnO powder electrode: (a) MnO, (b) C/MnO at a rate of 50 mA $g^{-1}$, and the corresponding capacity differential curves, (c) MnO, and (d) C/MnO.

The rate performances of the MnO and the C/MnO electrode are shown in Fig. 5. For the two samples, about 600 mAh $g^{-1}$ capacity at a rate of 400 mA $g^{-1}$ can be achieved, which is significantly improved compared with our previous report, only 400 mAh $g^{-1}$ can be obtained at the rate of 400 mA $g^{-1}$ [12]. The improvement could be related to the spherical morphology and the existence of pores among the primary particles. Carbon coating is not very effectively to improve the rate performance. This indicates that the electronic wetting is not the rate determining step in the conversion reaction. Fig. 6 shows a good cyclic performance of the C/MnO electrode in a half lithium cell. After 50 cycles, the capacity retention is 88%.

### 3.3. Reaction mechanism of MnO with lithium

Based on previous investigation on the MnO electrode at different lithiated and delithiated states using HRTEM and XRD techniques, it was clear that the initial polycrystalline MnO is converted into the Mn/$Li_2O$ nanocomposite during discharging. The nanocrystalline MnO phase reappears after charging. During discharging, it is also observed that a 40–60 nm solid electrolyte interphase (SEI) layer formed on the lithiated MnO particles and decomposed slightly during charging [12]. The initial coulombic efficiency of the MnO electrode was 65%. Therefore, it is not very sure whether the formed Mn/$Li_2O$ nanocomposite converts back to MnO completely due to uncertain SEI behaviors. It is also not clear that the formed Mn/$Li_2O$ nanocomposite is a real mixture

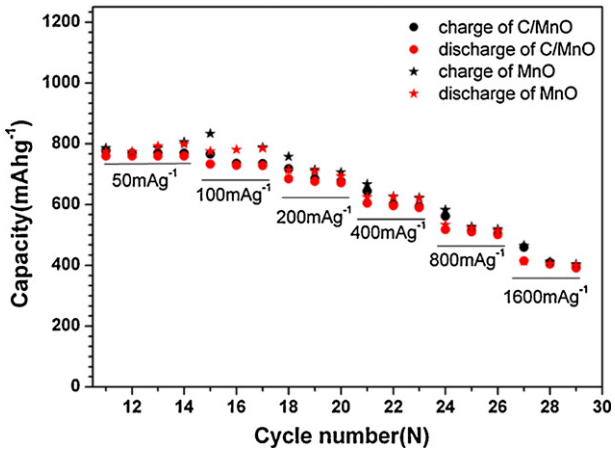


**Fig. 5.** Rate performances of the MnO and C/MnO electrode.

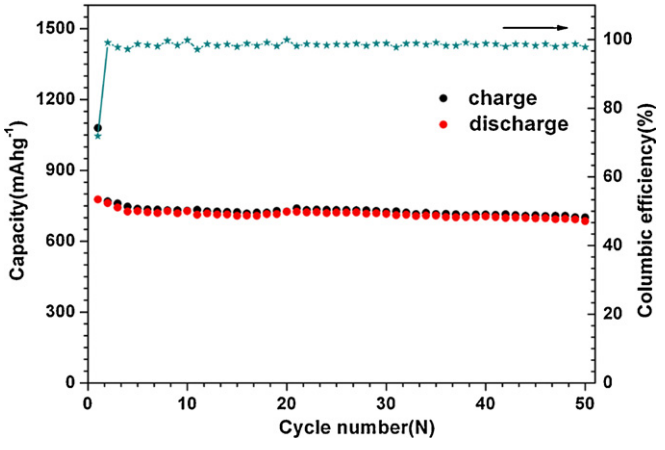


**Fig. 6.** Cyclic performance and coulombic efficiency of the C/MnO electrode at a rate of 50 mA $g^{-1}$.

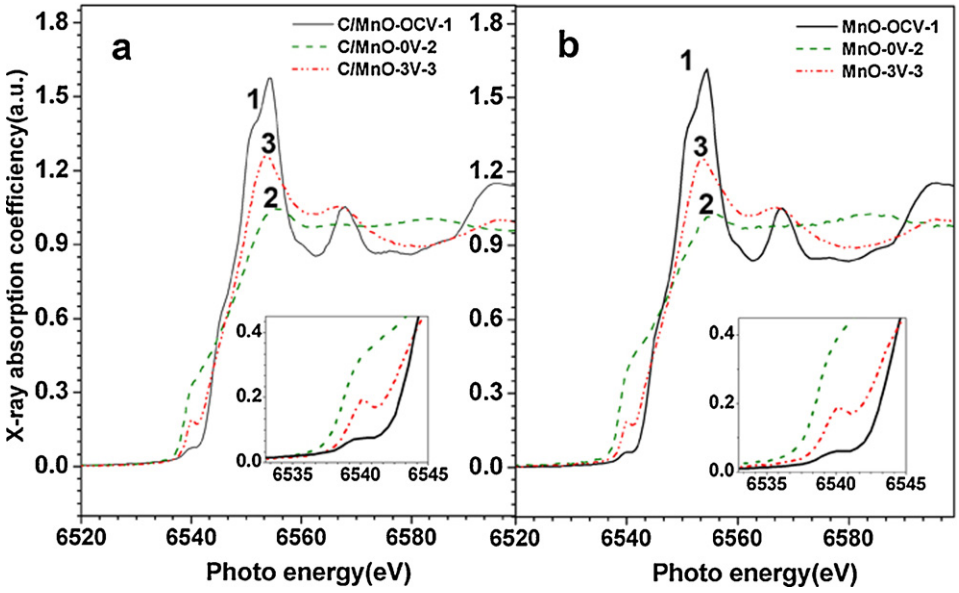


**Fig. 7.** The normalized Mn K-edge XANES spectra: (a) the C/MnO electrode, (b) the MnO electrode with different lithiated states. Black line: initial electrode, red line: discharging to 0 V, olive line: charging to 3 V. The inset shows the detail of the pre-edge region of the C/MnO and the MnO electrode with different lithiated states. (For interpretation of the references to color in this figure caption, the reader is referred to the web version of the article.)

of Mn and $Li_2O$ phase or a certain unknown intermediate phase, i.e., –Mn–O–Li–O–. Therefore, it is necessary to look at the local structure variation. Such investigation has rarely been done in conversion reactions and is difficult for most of techniques. X-ray absorption fine structure spectroscopy has been widely used to study the local structure around manganese and directly measure the redox state. Many authors have reported a shift of the edge positions (measured either at the inflection point or "halfway") for a systematically selection of model compounds of manganese [19–22], which indicates that the correlating between the edge position and the redox state of Mn is feasible.

The Mn K-edge XANES spectra of the C/MnO electrode and MnO electrode with different lithiated states are displayed in Fig. 7. (It has to be pointed out that the electrodes used for synchrotron X-ray absorption experiment showed the same capacity and columbic efficiency with the above indicated electrochemical performance.) As can be seen, the XANES spectra of the pristine C/MnO and MnO display a small pre-edge peak around 6539 eV. This is the 1*s* to 3*d* transition, which is normally forbidden and can only be allowed due to the hybridization of the *p* and *d* orbits. This spectrum is typical for MnO [23]. After discharged to 0 V, the pre-edge peak disappeared and the Mn K-edge position shifted to lower energy due to the decrease of the oxidation state of Mn ions. At this stage, the spectrum is very similar to that of the metallic Mn [24]. After recharging to 3 V, the pre-edge peak re-appeared again and the edge position of the fully charged state (3 V) is the same as that of the pristine composite, The edge position with different lithitated states measured at the inflection point are shown in Table 2 with deviations of 0.1–0.2 eV, which are well agreed with the reported redox state of Mn [23–25]. However, it also can be observed that at the discharging to 3 V stage, the pre-edge feature is much more dominant compared with that of the pristine one as the insets of Fig. 7a and b shows. Since pre-edge feature appears much less affected by the changes in the medium and long range environment than the main edge region, which was largely varied by constructive and destructive interferences (single and multiple scattering) arising from more distant neighbors around the central manganese atoms. Through *ab initio* calculation, F. Farges suggested that pre-edge intensity increases when $Mn^{2+}$ is located in the highly distorted octahedral symmetry, but also with redox state as more empty 3*d* levels are created by the ionization [26]. Thus, the coordination environment of the Mn ions (charged to 3 V) is more distorted compared with that of the pristine C/MnO. A careful view of the XANES spectra of the fully charged material and that of the pristine one, there are three oscillation peaks around 6555 eV, 6566 eV and 6590 eV. However, the oscillations of the fully charged one is much weaker compared with that of the pristine one, suggesting that the fully charged one is less crystalline MnO.

The Mn K-edge Fourier-transformed EXAFS spectra of the C/MnO with different lithiated states are displayed in Fig. 8. As can be seen, the spectrum of the pristine MnO/C displays mainly

**Table 2**
Edge position of normalized Mn K-edge XANES spectra of (a) C/MnO and (b) MnO with different discharge/charge depth.

| | OCV | 0 V | 3 V |
|---|---|---|---|
| C/MnO | 6543.9 eV | 6539.0 eV | 6543.0 eV |
| MnO | 6544.0 eV | 6539.0 eV | 6543.0 eV |

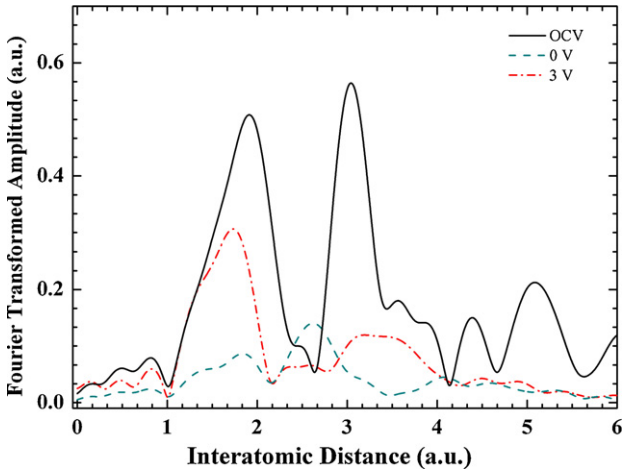


**Fig. 8.** Fourier transformed magnitudes (FT) of EXAFS for C/MnO. (a) Initial electrode, (b) discharging to 0 V, and (c) charging to 3 V.

two peaks below 4 Å, which are located around 1.9 Å and 3.0 Å, respectively. These two peaks correlated to the Mn–O interaction in the first coordination shell and Mn–Mn interaction in the second coordination shell, respectively. This is consistent with that of the standard MnO. After discharged to 0 V, the Fourier transformed Mn K-edge spectrum displays two peaks around 1.9 Å and 2.7 Å. The peak located at 2.7 Å is the Mn–Mn interaction of the metallic Mn and the peak located at 1.9 Å is the Mn–O interaction of the residual MnO. The residual MnO in fully discharged state is not likely to be caused by the unreacted MnO, but could be caused by the reaction of formed Mn nanograin with trace amount of oxygen in the glove box.

After recharging to 3 V, the intensity of the Mn–O peak (1.9 Å) increased and the intensity of the peak located at 2.7 Å largely decreased, but not completely disappeared, which is essentially the interaction of the Mn–Mn in the metallic Mn, it indicates that part of reduced $Mn^0$ is not oxidized to $Mn^{2+}$ after charging to 3 V. Compared the spectra of the pristine C/MnO and the fully charged C/MnO, they all displayed the Mn–O and Mn–Mn interactions, as mentioned earlier. However, the intensity ratio of these two peaks is quite different. Especially, the intensity of the Mn–Mn interaction of the C/MnO at the fully charged stage is much weaker compared with that of the pristine C/MnO, indicating that the Mn–Mn distribution for the fully charged material is not so regular in the second shell, and is consistent with the XANES observations and our previous *ex situ* XRD and TEM (the fully charged one is less crystalline MnO). The Mn–O bond distance of the fully charged C/MnO is also shorter compared with that of the pristine one. This indicates that Mn ions are located in more distorted octahedra in the oxidized C/MnO (3 V).

### 3.4. Thermodynamic and kinetic property

Through the above discussion and our previous report [12], we confirmed that initial polycrystalline MnO was found to be converted into a $Li_2O$/Mn nanocomposite after a full insertion of lithium. Then the nanocomposite partially converted back into nanocrystalline MnO upon lithium extraction [12]. Such a microstructure variation has also been observed in many transitional metal compounds through the conversion reactions. The reaction formula at the first insertion, the first extraction and the second insertion can be written as following:

$$MnO_{polycrystalline} + Li \rightarrow Li_2O_{nano}/Mn_{nano} \quad (1)$$

$$Li_2O_{nano} + Mn_{nano} \rightarrow MnO_{nanocrystalline} + Li \quad (2)$$

$$MnO_{nanocrystalline} + Li \rightarrow Li_2O_{nano}/Mn_{nano} \quad (3)$$

From the galvanostatic intermittent titration technique (GITT) result shown in Fig. 9. It is observed that the open circuit voltage of the MnO electrode varies with lithiation depth and cycles [12]. The emf values of the reactions (1)–(3) can be calculated from the Nernst equations:

$$-nE_1F = \Delta_r G_1 = (\Delta_F G(Li_2O_{nano}) + \Delta_F G(Mn_{nano}) - \Delta_F G(MnO_{polycrystalline})) \quad (4)$$

$$-nE_2F = \Delta_r G_2 = (\Delta_F G(MnO_{nanocrystalline}) - \Delta_F G(Li_2O_{nano}) - \Delta_F G(Mn_{nano})) \quad (5)$$

$$-nE_3F = \Delta_r G_3 = (\Delta_F G(Li_2O_{nano}) + \Delta_F G(Mn_{nano}) - \Delta_F G(MnO_{nanocrystalline})) \quad (6)$$

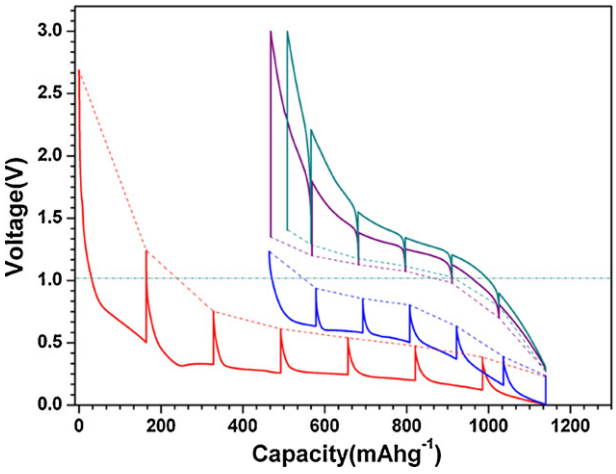


**Fig. 9.** GITT curves of the MnO powder electrode. Relaxation time is 64 h. Solid lines are GITT result, dash lines are open circuit voltage, dot dash line is the emf value calculated from bulk materials. Redraw from Ref. [12].

The voltage difference between the first discharge and second discharge is related to the formation energy difference between the initial MnO polycrystalline and the converted MnO nanocrystalline:

$$\Delta E_{d2-d1} = E_3 - E_1 = \frac{\Delta_F G(MnO_{nanocrystalline}) - \Delta_F G(MnO_{polycrystalline})}{2F} \quad (7)$$

The origin of this kind of voltage difference has been discussed by Delmar et al. in terms of surface energy and amorphorization effect in the case of $RuO_2$ [27]. In principle, the voltage difference between the first charge and the second discharge ($\Delta E_{d2-c1} = E_3 - E_2$) in the conversion reaction region should be zero. However, significant voltage difference can be seen in Fig. 9 [12]. Recently, Doe et al. explained the origin of the voltage hysteresis of the $FeF_3$ electrode at 1/200*C* [28]. The first principle calculations indicate that the reaction paths of lithium insertion and extraction could be different under nonequlibrium states by selecting different kinetic favorable intermediate products $Li_xFe_yF_3$. The existence of a 5 mV voltage difference between the discharging and charging curves at zero current density has also been noticed in the case of $LiFePO_4$ [29]. This difference is explained by the many particle effect.

Since the emf value of the real system occurring conversion reaction is very difficult to be measured and predicted, the sum of the overpotential during charging and discharging can be taken by selecting the middle point of the voltage profiles in the conversion reaction region [12]. A summary of this type of behaviors for the MnO and the C/MnO electrodes, in addition to our previous reported four materials (the carbon coated and uncoated irregular MnO-based materials) [12], is shown in Fig. 10. Here, MnO-L represents micron size MnO from commercial product, MnO-S represents nano-sheet MnO obtained by high energy ball milling. The detailed morphology can be seen in our previous report [12]. It can be seen that the electrode polarization in all cases obeys ohmic rule in this current density range (not Tafel type). However, the intercept value at *y* axis is a nonzero value of 0.75–0.8 V as if a zero-current overpotential exists. It is believed that the origin of this value is related to thermodynamic factor, as shown in the GITT results. Decreasing particle size and carbon coating can only partially decrease the voltage polarization, cannot influence the zero-current overpotential significantly.

In the case of MnO, the voltage hysteresis is very large. It seems that no any intermediate $Li_xMnO$ compounds could exist based on *ex situ* TEM, XRD, XANES and EXAFS investigation. Therefore, the appearance of this large voltage difference in the OCV curves and 0.75 V zero current overpotential should be originated from other thermodynamic factor. When the MnO phase is converted into the

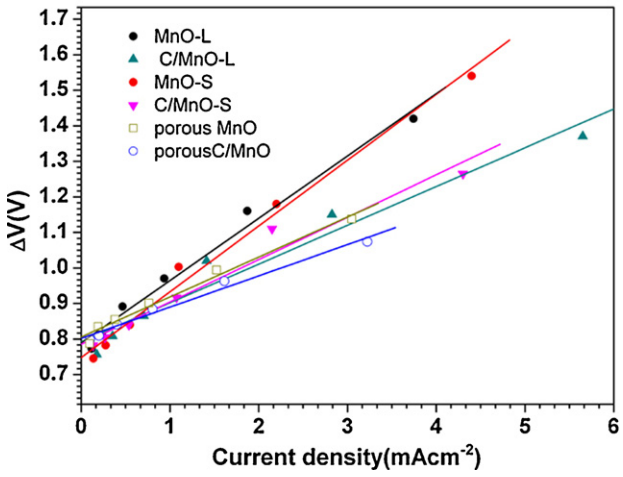


**Fig. 10.** The voltage difference between the first charge and the second discharge in the galvanostatic voltage profile of Li/MnO cell at different current densities. $\Delta V$ is taken from the middle of the voltage plateau in conversion reaction region between the charging curve and the discharging curve.

$Li_2O$/Mn phase, it leads to a 170% volume expansion at least (calculated from the volume difference between crystal MnO and the volume sum of crystal $Li_2O$ and Mn). The lithium extraction will occur in a reverse situation. Such a volume variation will lead to energy difference in terms of $P\Delta V$ and the surface energy. Quantitatively estimation of these contributions is still not possible due to absence of thermodynamic data. Further thermodynamic and kinetic investigations are carrying out for clarifying above interesting issues.

## 4. Conclusion

MnO microspheres were prepared as anode materials for lithium ion batteries, which show a reversible capacity of 800 mAh $g^{-1}$ and an initial efficiency of 71%. It can deliver 600 mAh $g^{-1}$ at a rate of 400 mA $g^{-1}$. According to *ex situ* XANES and EXAFS investigation, it seems that MnO is decomposed into Mn/$Li_2O$ after discharging to 0 V and no intermediate phase is observed. The reduced $Mn^0$ is oxidized to $Mn^{2+}$ partially. This explains the origin of the initial irreversible capacity loss and lower reversible capacity partially. Decreasing particle size and carbon coating can only partially decrease the voltage polarization, cannot influence the voltage hysteresis or so-called zero-current overpotential significantly.

## Acknowledgements

This work was supported by NSFC (50730005), CAS (KJCX2-YW-W26), "863" project (2009AA033101) and "973" project (2007CB936501). Dr. Wen Wen thank the Shanghai Institute of Applied Physics, CAS for the financial support (O95501E061). Technical support of Dr. Xiangjun Wei is appreciated. The authors also thank the BL14W of Shanghai Synchrotron Radiation Facility for providing the beamtime.

## References

[1] P. Poizot, S. Laruelle, S. Grugeon, L. Dupont, J.M. Tarascon, Nature 407 (2000) 496–499.
[2] H. Li, G. Richter, J. Maier, Adv. Mater. 15 (2003) 736–739.
[3] F. Badway, N. Pereira, F. Cosandey, G.G. Amatucci, J. Electrochem. Soc. 150 (2003) A1209–A1218.
[4] P. Poizot, S. Laruelle, S. Grugeon, L. Dupont, J.M. Tarascon, J. Electrochem. Soc. 149 (2002) A1212–A1217.
[5] N. Pereira, L.C. Klein, G.G. Amatucci, J. Electrochem. Soc. 149 (2002) A262–A271.
[6] D.C.C. Silva, O. Crosnier, G. Ouvrard, J. Greedan, A. Safa-Sefat, L.F. Nazar, Electrochem. Solid-State Lett. 6 (2003) A162–A165.
[7] Y. Wang, Z.W. Fu, X.L. Yue, Q.Z. Qin, J. Electrochem. Soc. 151 (2004) E162–E167.
[8] A. Débart, L. Dupont, P. Poizot, J.B. Leriche, J.M. Tarascon, J. Electrochem. Soc. 148 (2001) A1266–A1274.
[9] P. Balaya, H. Li, L. Kienle, J. Maier, Adv. Funct. Mater. 13 (2003) 621–625.
[10] H. Li, P. Balaya, J. Maier, J. Electrochem. Soc. 151 (2004) A1878–A1885.
[11] X.Q. Yu, Y. He, J.P. Sun, K. Tang, H. Li, L.Q. Chen, X.J. Huang, Electrochem. Commun. 11 (2009) 791–794.
[12] K. Zhong, X. Xia, B. Zhang, H. Li, Z.X. Wang, L.Q. Chen, J. Power Sources 195 (2010) 3300–3308.
[13] J. Liu, Q.M. Pan, Electrochem. Solid State Lett. 13 (2010) A139–A142.
[14] B. Ravel, M. Newville, J. Synchrotron Rad. 12 (2005) 537–541.
[15] H.H. Chou, H.Y. Fan, Phys. Rev. B 12 (1976) 3924–3937.
[16] F. Kapteijn, A.D. van Langeveld, J.A. Moulijn, A. Andreini, J. Catalysis 150 (1994) 94–104.
[17] K. Ramesh, L.W. Chen, F.X. Chen, Y. Liu, Z. Wang, Y.F. Han, Catal. Today 131 (2008) 477–482.
[18] N. Mironova-Ulmane, A. Kuzmin, M. Grube, J. Alloys Compd. 480 (2009) 97–99.
[19] A. Manceau, A. Gorshkov, V. Drits, Am. Miner. 77 (1992) 1133–1143.
[20] D.A. Mckeown, J.E. Post, Am. Miner. 86 (2001) 701–713.
[21] J.R. Bargar, B.M. Tebo, J.E. Villinski, Geochim. Cosmochim. Acta 64 (2000) 2775–2778.
[22] D.A. McKeown, W.K. Kot, H. Gan, I.L. Pegg, J. Non- Cryst. Solids 328 (2003) 71–89.
[23] K.W. Nam, M.G. Kim, K.B. Kim, J. Phys. Chem. C 111 (2007) 749–758.
[24] G.N. Greaves, P.J. Durham, G. Diakun, P. Quinn, Nature 294 (1981) 139–142.
[25] G. Drager, T. Kirchner, S. Bocharov, C.C. Kao, J. Synchrotron Radiat. 8 (2001) 398–400.
[26] F. Farges, Phys. Rev. B 71 (2005) 155109.
[27] O. Delmer, P. Balaya, L. Kienle, J. Maier, Adv. Mater. 20 (2008) 501–505.
[28] R.E. Doe, K.A. Persson, Y.S. Meng, G. Ceder, Chem. Mater. 20 (2008) 5274–5283.
[29] W. Dreyer, J. Jamnik, C. Guhlke, R. Huth, J. Moškon, M. Gaberšček, Nat. Mater. 9 (2010) 448–453.